CIRP Journal of Manufacturing Science and Technology 55 (2024) 16–27

Contents lists available at ScienceDirect

CIRP Journal of Manufacturing Science and Technology

journal homepage: www.elsevier.com/locate/cirpj

Process damping force model calibration using in situ velocity

Dylan Pollard [a], Jose Nazario [a], Junbeom Son [a], Tyler Woodard [a], Michael Gomez [b], Tony Schmitz [a,c,*]

[a] Department of Mechanical, Aerospace, and Biomedical Engineering, University of Tennessee, Knoxville, Knoxville, TN, USA [b] Manufacturing Research and Technology, MSC Industrial Supply Co., Davidson, NC, USA [c] Manufacturing Demonstration Facility, Oak Ridge National Laboratory, Knoxville, TN, USA

ARTICLEINFO

Keywords:
Machining
Modeling
Process damping
Chatter

ABSTRACT

This paper describes a process damping force model calibrated using an in situ measurement of velocity during an unstable milling test. The process damping coefficient is selected to match simulated and measured velocity signals. The coefficient is inserted in the cutting force model and time-delay differential equations of motion that describe the milling system. The modeling approach is described and experimental results are presented for: 1) selecting the process damping coefficient; and 2) comparing measured velocities and milling stability to predictions from time domain simulation.

1. Introduction

Modeling the dynamic performance of machining operations remains an important research topic [1]. Process model inputs typically include the tool and workpiece structural dynamics, represented by frequency response functions, or FRFs; mechanistic cutting force coefficients that depend on the workpiece material, tool geometry and material, and coolant/lubricant application, if any; and machining parameters, such as radial depth of cut, cutting direction (up or down), and feed per tooth for milling [2]. Machining dynamics model predictions include the boundary between stable and unstable (chatter) combinations of spindle speed and axial depth for milling; surface location error due to forced vibrations during stable milling; and time-dependent cutting force and tool/workpiece displacements during material removal. Modeling approaches include time domain, frequency domain, and semi-discretization [3].

Despite the significant advances in modeling machining operations over the past decades, process damping remains a topic of interest. Early efforts by Sisson and Kegg [4] and Wallace and Andrew [5] explained the increase in stability observed at low cutting speeds as dynamic interference between the relief/flank and machined surfaces with associated energy dissipation. Follow-on efforts examined cutting force models and setups to experimentally identify the model coefficients for new and worn tools [6–13]. More recently, deterministic and machine learning milling models that represent the process damping effect using experimental cutting force coefficient(s) have been reported and evaluated [14–27].

Altintas et al. [28] presented a process damping force model and piezoelectric actuator to calibrate the model coefficients. The coefficients were determined using a combination of force and tool displacement measurements during orthogonal plunge turning tests. As suggested by Das and Tobias [29], the process damping contribution was partially calculated as the product of a coefficient, the axial depth of cut, and the ratio of the relative velocity between the tool and workpiece to the cutting speed. This calibration approach is an alternative to the geometric approach suggested by Lee et al. [30] and others, where the process damping force components are calculated by estimating the volumetric interference between the tool relief/flank and machined surface, as well as a dry sliding friction coefficient.

The approach presented here builds on these prior efforts by proposing a velocity measurement during unstable milling conditions. The measured velocity is used to calibrate a process damping coefficient that is included within the force model and time-delay differential equations of motion that describe the milling system. The paper is organized as follows. First, the modeling approach is described. Second, the experimental setup is detailed. Third, results are provided. Fourth, conclusions are presented.

2. Modeling approach

In the proposed solution, in situ velocity measurements for milling are compared to velocity predictions using time domain simulation,

* Corresponding author at: Department of Mechanical, Aerospace, and Biomedical Engineering, University of Tennessee, Knoxville, Knoxville, TN, USA. *E-mail address:* tony.schmitz@utk.edu (T. Schmitz).

https://doi.org/10.1016/j.cirpj.2024.09.001

Received 4 May 2024; Received in revised form 18 July 2024; Accepted 1 September 2024 Available online 10 September 2024 1755-5817/

where the milling equations of motion are solved numerically in small time steps [2,31]. A single process damping coefficient is calibrated by matching the measured and simulated velocities. The time domain

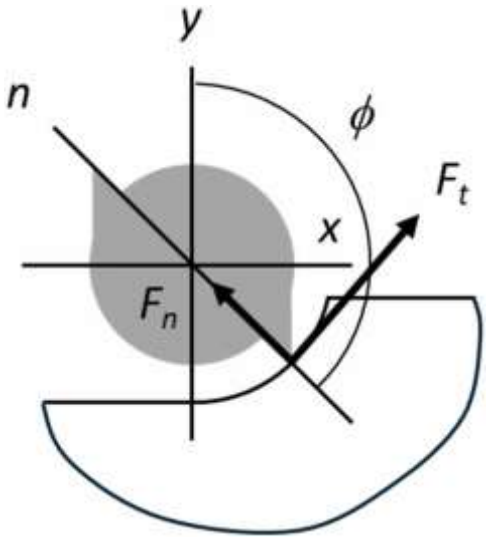

Fig. 1. Milling simulation geometry. The normal and tangential direction cutting force components, F_n and F_t, are identified. The fixed x (feed) and y directions, as well as the rotating surface normal direction, n, are also shown. The angle ϕ defines the tooth angle. The tool feed is to the right for the clockwise tool rotation and the axial depth is in the z direction.

Table 1
Modal parameters for the tool and platform in the x and y directions.

Tool					
x			y		
f_n (Hz)	k (N/m)	ζ (%)	f_n (Hz)	k (N/m)	ζ (%)
929	1.90×10^8	1.49	497	8.28×10^7	5.72
959	2.33×10^7	3.96	920	6.94×10^7	2.94
1160	1.34×10^8	3.15	978	1.57×10^7	7.11
1286	8.12×10^6	6.19	1110	3.41×10^7	3.25
1493	5.96×10^7	2.41	1160	8.90×10^7	1.29
1604	4.29×10^7	2.62	1323	4.27×10^7	7.70
1737	1.50×10^7	2.85	1607	9.88×10^6	3.81
1815	1.11×10^8	1.00	1727	1.83×10^8	0.73
1912	2.68×10^7	4.50	1766	1.39×10^7	2.49
2265	1.41×10^8	2.89	2031	6.40×10^7	9.03
Platform x			y		
f_n (Hz)	k (N/m)	ζ (%)	f_n (Hz)	k (N/m)	ζ (%)
766	1.93×10^7	0.54	294	7.88×10^8	3.88
			520	1.06×10^9	26.1
			1250	2.73×10^9	4.46
			1889	1.56×10^9	5.95
			2663	3.11×10^8	4.55

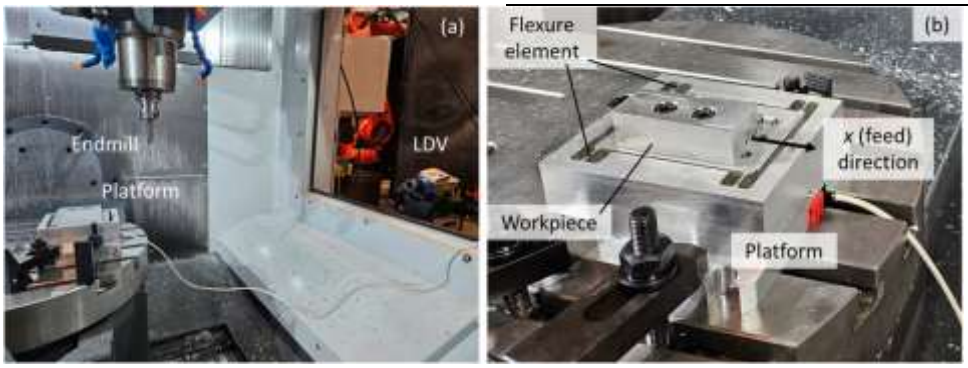

Fig. 2. (a) Experimental setup showing the platform clamped to the machining center table, endmill and holder inserted in the spindle, and LDV for workpiece velocity measurement in the x direction. (b) The platform is shown and the workpiece and flexure elements are identified.

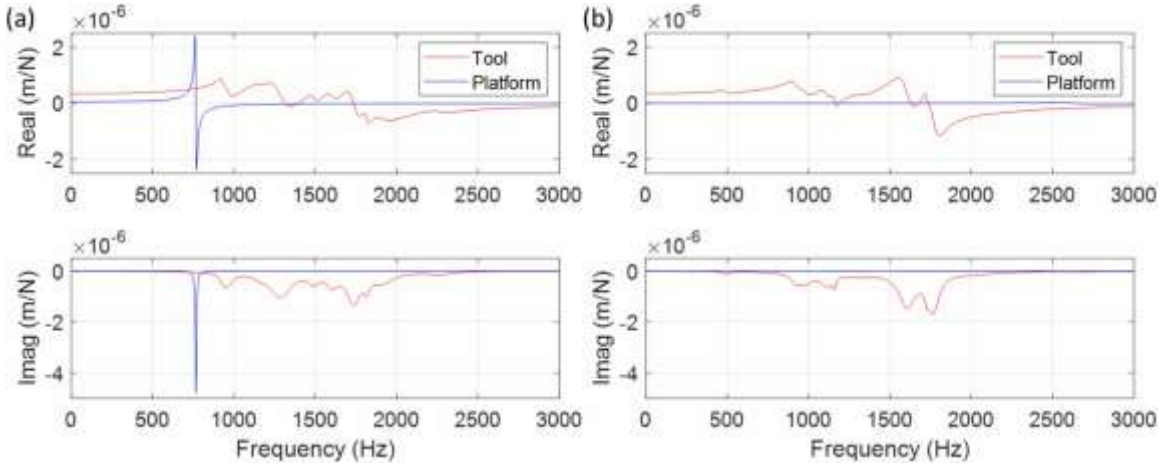

Fig. 3. (a) Real (top panel) and imaginary (bottom panel) parts of the x direction FRFs for the tool and platform. (b) Real and imaginary parts of the y direction FRFs. It is observed that the platform provides a single degree of freedom FRF in the x direction and the tool has multiple vibrations modes with asymmetric FRFs between the x and y directions. The platform y direction modes cannot be observed at this scale, but are present.

Table 2
Cutting force coefficient values for tool- workpiece combination.

Coefficient	Value
k_{tc} (N/mm2)	1015

k_{te} (N/mm) k_{nc} (N/mm2)	356 10.3
k_{ne} (N/mm)	11.8

simulation and calibration approach are described in the following sections.

2.1. Time domain simulation

The time domain simulation used in this study is based on Fig. 1 and proceeds as follows. The instantaneous chip thickness, h, is determined using the commanded chip thickness, vibration of the current tooth in the surface normal direction, and vibration of the previous tooth in the normal direction at the selected tooth angle, ϕ. The cutting force components in the tangential, t, and normal, n, directions are calculated using the instantaneous chip thickness as shown in Eqs. (1) and (2), where b is the axial depth of cut and the cutting force coefficients, k, are identified by the subscripts t or n for direction and c or e for cutting or edge effect. In Eq. (2), the final term represents process damping, where C is the process damping coefficient (N/m), V is the cutting speed (m/s), and $\dot{n}$ is the relative velocity between the tool and workpiece in the normal direction (m/s).

$$F_t = k_{tc}bh + k_{te}b \quad (1)$$

$$F_n = k_{nc}bh + k_{ne}b - C\frac{b}{V}\dot{n} \quad (2)$$

The two cutting force components are used to find the new displacements by numerical integration of the time-delay differential equations of motion in the x (feed) and y directions as shown in Eqs. (3) and (4), where m is the modal mass, c is the modal viscous damping coefficient, and k and the modal stiffness. The subscripts identify the direction and multiple degrees of freedom in each direction can be accommodated. Eqs. (3) and (4) are solved for both the tool and workpiece, where the modal parameters are different, but the same force components (with opposite directions) are applied to both. A modified Euler numerical integration strategy with a fixed time step was applied to solve the equations of motion. The time step was selected to be 5 % of the smallest period (corresponding to the largest natural frequency) for all vibration modes used to describe the tool and workpiece dynamics. Zero initial conditions were applied in all cases. It is recognized, however, that variation in simulation output with changing initial conditions is an indication of nonlinear behavior as studied by Dombovari et al. [32], Moradi et al. [33], and others.

$$m_x\ddot{x} + c_x\dot{x} + k_x x = -F_t\cos(\phi) - F_n\sin(\phi) \quad (3)$$

$$m_y\ddot{y} + c_y\dot{y} + k_y y = F_t\sin(\phi) - F_n\cos(\phi) \quad (4)$$

The tool rotation angle is then incremented and the process is repeated. The instantaneous chip thickness depends on the commanded, tooth angle-dependent chip thickness, the current vibration in the direction normal to the surface, and the vibration of previous teeth at the same tooth angle. The chip thickness is calculated using the circular tooth path approximation as described by Eq. (5), where f_t is the

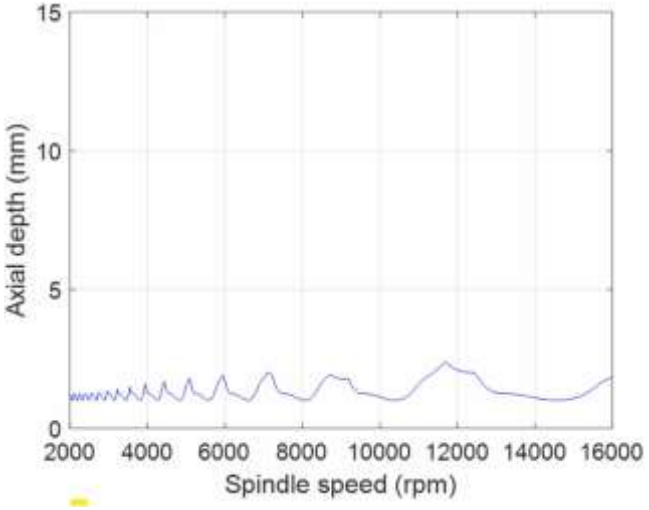

Fig. 5. Zero-order frequency domain algorithm stability map.

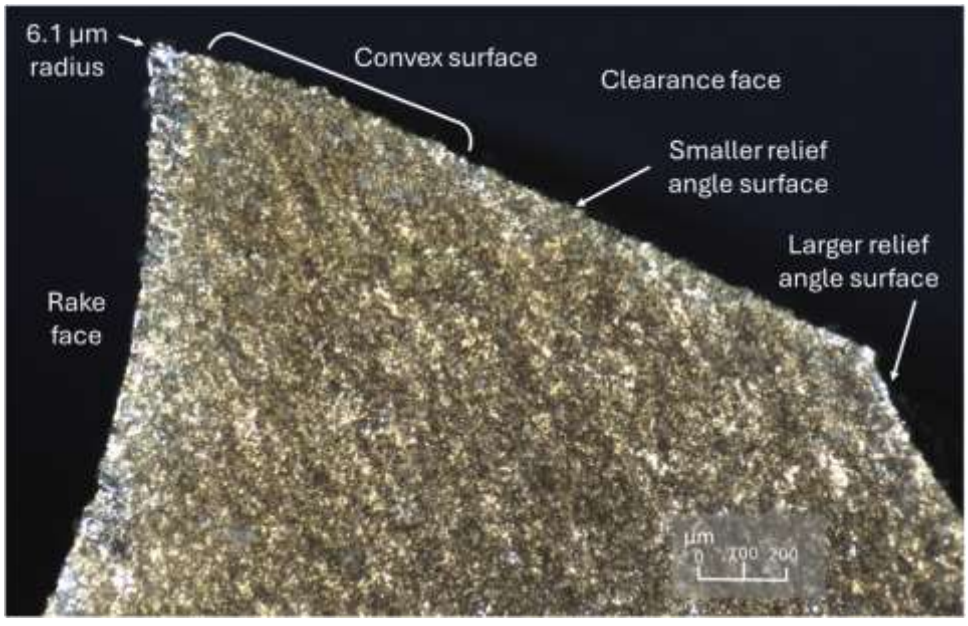

Fig. 4. Cross-section of endmill cutting edge. The rake and clearance faces are identified and the clearance face geometry is described.

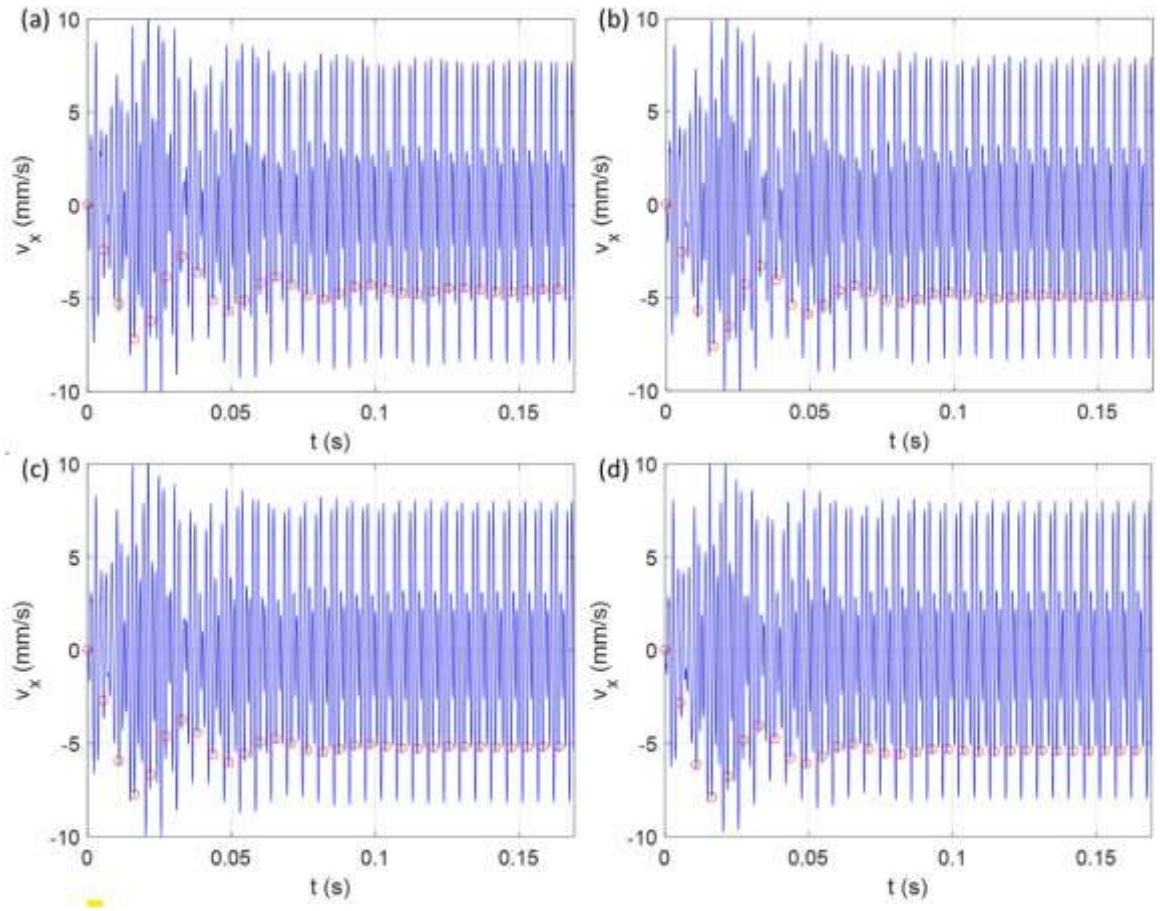

Fig. 6. Variation in v_x with C for {Ω, b} = {11000 rpm, 1 mm} and C = (a) 0, (b) 2×10^5 N/m, (c) 4×10^5 N/m, and (d) 6×10^5 N/m. The red circles represent once-per-revolution samples. After the initial transients attenuate, the samples repeat which indicates forced vibration and stable cutting conditions.

commanded feed per tooth, n is the normal direction (see Fig. 1), τ is the tooth period which introduces the time delay, RO is the tooth dependent runout (i.e., the radius difference between teeth), and the time dependence is included.

$$h(t) = f_t \sin(\phi) + n(t - \tau) - n(t) + RO \quad (5)$$

The tooth period (seconds) is defined by Eq. (6), where Ω is the spindle speed (rpm) and N_t is the number of teeth.

$$\tau = \frac{\Omega}{60 N_t} \quad (6)$$

The normal direction displacement for the current tooth depends on the tool (T) and workpiece (W) x and y direction displacements as well as the tooth angle as shown in Eq. (7). The velocity in the normal direction is given by Eq. (8), where the overdot indicates the time derivative.

$$n = -(x_T - x_W)\sin(\phi) - (y_T - y_W)\cos(\phi) \quad (7)$$

$$\dot{n} = -(\dot{x}_T - \dot{x}_W)\sin(\phi) - (\dot{y}_T - \dot{y}_W)\cos(\phi) \quad (8)$$

For the simulation, the tool orientation angles are divided into a discrete number of steps. At each time step, dt, the cutter angle is incremented by the corresponding small angle, $d\phi$. This approach enables convenient computation of the chip thickness for each simulation step because: 1) the teeth orientations are predefined; and 2) the surface created by the previous teeth at each angle are stored. The cutter rotation (radians) depends on the selection of the number of steps per revolution, SR, as shown in Eq. (9).

$$d\phi = \frac{2\pi}{SR} \quad (9)$$

The corresponding time step (seconds) is defined in Eq. (10).

$$dt = \frac{60}{SR \cdot \Omega} \quad (10)$$

A vector of angles is defined to represent the potential orientations of the teeth as the cutter is rotated through one revolution of the circular tool path, $\phi = [0, d\phi, 2\,d\phi, 3\,d\phi, \ldots, (SR - 1)\,d\phi]$. The rotating teeth orientations within the cut are then defined by referencing entries in this vector.

To accommodate the helix angle, γ, for the tool's cutting edges, the tool is sectioned into axial slices. Each slice is treated as an individual straight tooth endmill, where the thickness of each slice is a small fraction, db, of the axial depth. Each slice incorporates a circumferential distance delay relative to the prior slice (nearer the cutter free end) as shown in Eq. (11), where r is the endmill radius.

$$r\chi = db\tan(\gamma) \quad (11)$$

The angular delay (radians) between slices for the rotating endmill is then defined by Eq. (12).

$$\chi = \frac{db\tan(\gamma)}{r} \quad (12)$$

To ensure that the angles for each axial slice match the predefined tooth angles, the delay angle between slices is $\chi = d\phi$. This places a constraint on the db value. By substituting $d\phi$ for χ and rearranging, the required slice width is provided in Eq. (13).

$$db = \tan(\gamma) r \cdot d\phi \quad (13)$$

Fig. 7. Variation in v_x with C for {11,000 rpm, 5 mm} and C = (a) 0, (b) 2×10^5 N/m, (c) 4×10^5 N/m, and (d) 6×10^5 N/m. The once-per-revolution samples show

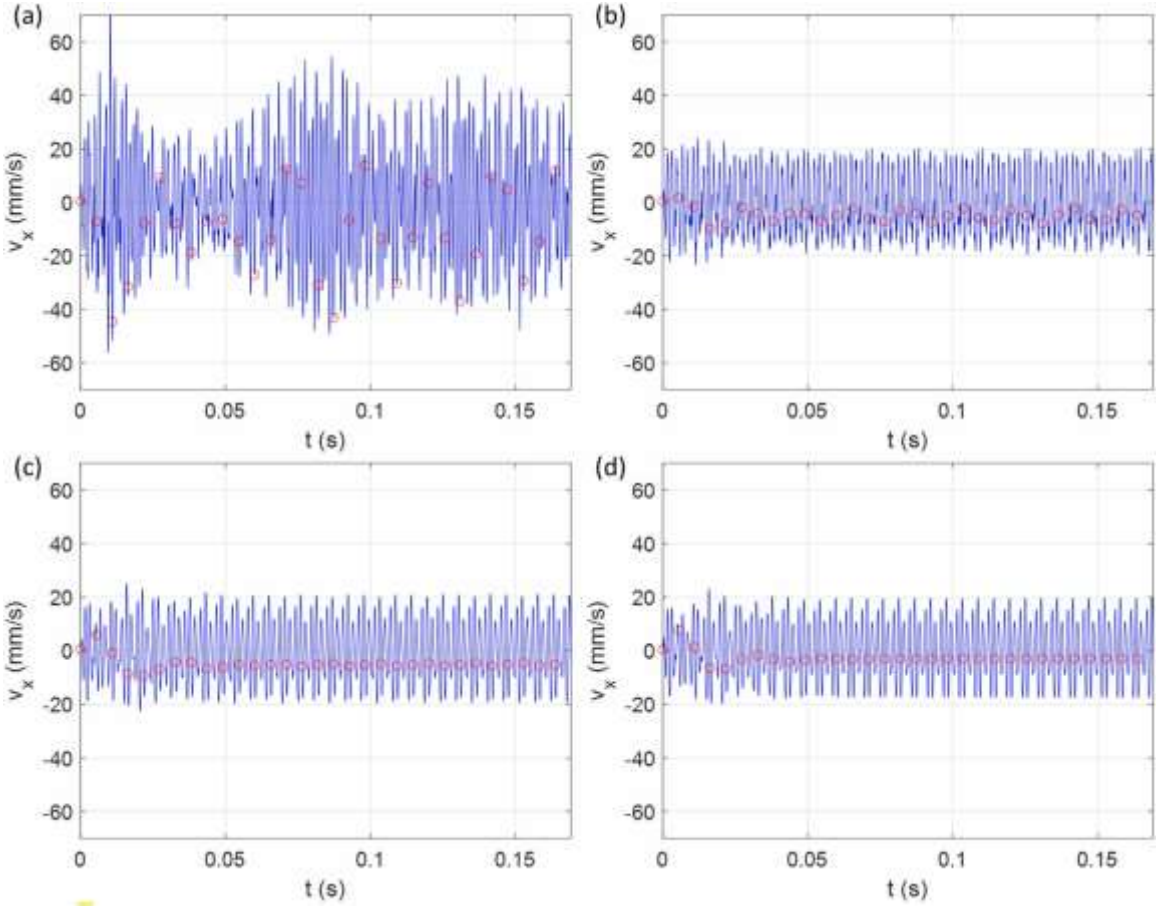

that (a) and (b) are unstable, (c) is marginally stable, and (d) is stable.

2.2. Process damping coefficient determination

Using the numerical milling simulation, the time-dependent cutting force components, displacements, velocities, and accelerations of the tool and workpiece are calculated. The simulated velocity is then compared to measured velocity for unstable cutting conditions. This approach is selected because, as shown in the Results section, the sensitivity of the velocity to the process damping coefficient is higher for unstable (chatter) conditions. By selecting the process damping coefficient to provide agreement between the simulated and measured velocities, the stability map can be predicted using the calibrated process damping coefficient for a grid of time domain simulations.

3. Experimental setup

The setup is displayed in Fig. 2, where the 7075 aluminum workpiece was mounted to a flexure-based platform [34] and the platform was clamped to the table of a five-axis machining center (Haas UMC-750). The platform was composed of a monolithic parallelogram leaf-type flexure to provide single degree of freedom motion, where the platform's flexible direction was aligned with the x (feed) direction. This enabled the workpiece velocity to be measured in situ by a laser Doppler vibrometer (LDV) and compared to the simulated workpiece velocity.

The platform dynamics were measured by tap testing and modal fitting was applied to identify the natural frequency, f_n, modal stiffness, k, and modal viscous damping ratio, ζ, for each vibration mode. A solid carbide endmill (Accupro part number 12182289) and ER32 collet holder (Accupro part number 525421) combination was selected to provide tool tip FRFs in the x and y directions with similar stiffness, but higher damping, compared to the platform. Again, tap testing and modal fitting were applied to identify the modal parameters for use in the time domain simulation. The FRFs for the platform and tool tip are shown in Fig. 3 (x direction) and 4 (y direction). The modal parameters are listed in Table 1.

The 12.7 mm diameter endmill used in this study had three equally spaced teeth, a 40 deg helix angle for each tooth, and runout values of {0, 1, and 9} µm. The k_{tc}, k_{te}, k_{nc}, and k_{ne} cutting force model coefficients from Eqs. (1) and (2) were determined using linear regressions to the mean cutting force in the x and y directions over a range of feed per tooth values [2]. Stable down milling with a 6.35 mm radial depth was selected for these cutting tests and no coolant/lubricant was used. The coefficient values are provided in Table 2.

Because the clearance face geometry is known to affect process damping behavior, the cutting edge geometry is displayed in Fig. 4. To obtain this image, the endmill was sectioned using electrical discharge machining (EDM) and a digital microscope was used to measure the cross-section geometry. It is observed that the rake angle constantly varies along the curved rake face and that two relief angles are included on the clearance face. For the smaller relief angle, the surface appears to be slightly convex near the 6.1 µm radius cutting edge and flat for the remainder of the surface. The surface is flat again for the larger relief angle.

4. Results

The tool and platform modal parameters from Table 1 and cutting force coefficients from Table 2 were applied to generate a down milling stability map using the zero-order frequency domain algorithm

Fig. 8. (a) Magnitude of frequency content for the measured workpiece velocity at {11,000 rpm, 10 mm}. The green circles identify the tooth passing frequency and its harmonics. (b) Comparison of measured and simulated workpiece v_x for $C = 4.33 \times 10^5$ N/m. (c) Predicted velocity with once-per-revolution sampling (red

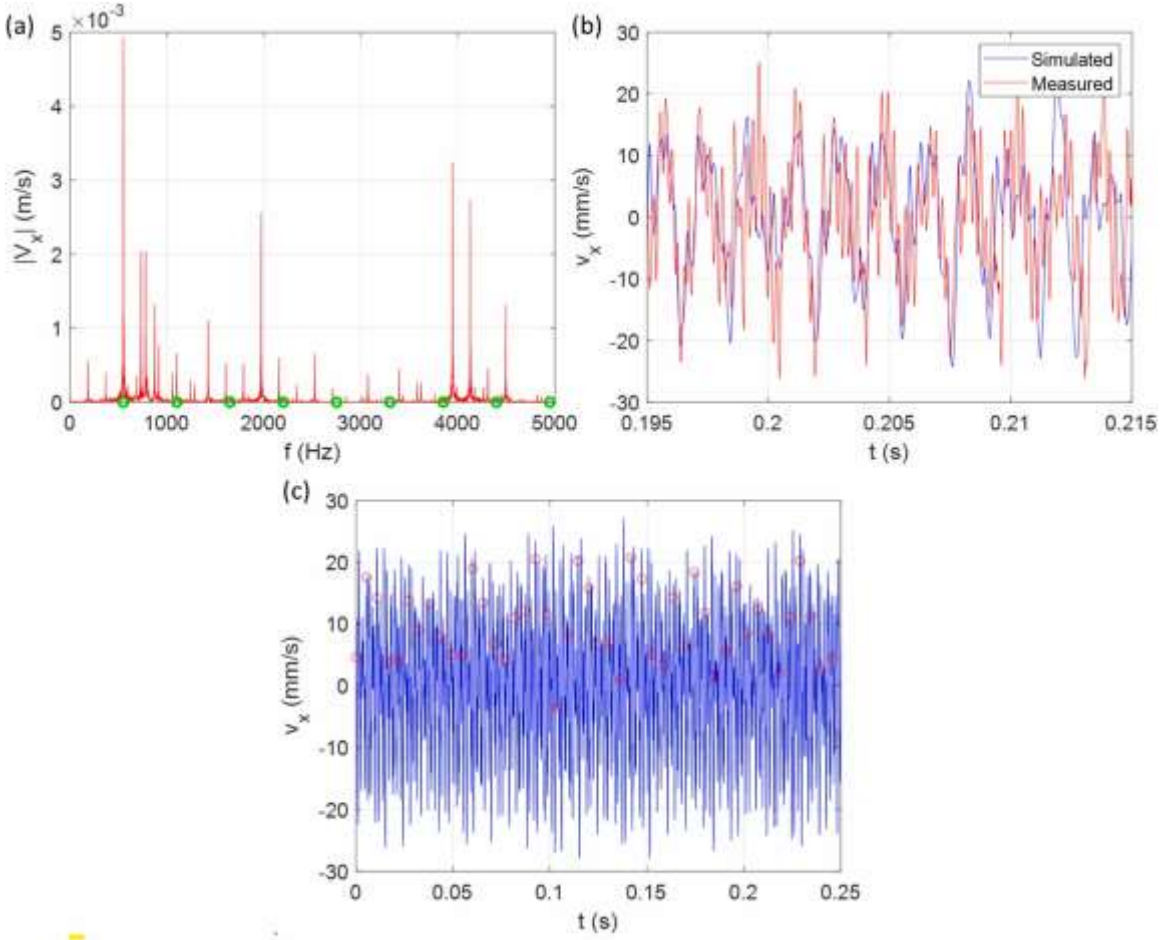

circles). Because the samples do not repeat, unstable behavior is identified.

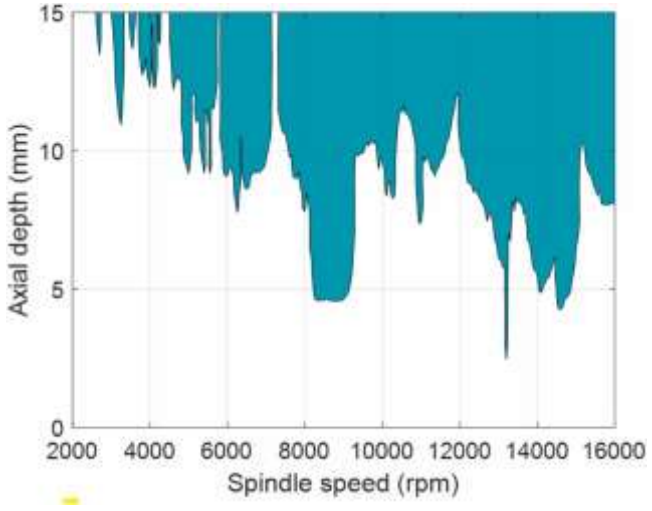

Fig. 9. Down milling stability map for $C = 4.33 \times 10^5$ N/m with a 6.35 mm radial depth.

described in [35]. The radial depth was 6.35 mm. While this algorithm does not include process damping effects, it does provide a starting point for selecting a calibration test point; see Fig. 5.

To select a test point for calibrating the process damping coefficient from Eq. (2), the sensitivity of the simulated workpiece velocity to the selected C value was evaluated for two axial depths of cut from Fig. 5: one below the stability boundary (blue curve) and one above. Fig. 6 displays the workpiece velocity in the x direction, v_x, for a 1 mm axial depth and four C values: {0, 2×10^5, 4×10^5, and 6×10^5} N/m. The spindle speed was 11,000 rpm, the feed per tooth was 0.025 mm, and the radial depth was 6.35 mm for the down milling simulations. It is observed that there is no significant change in v_x with C.

Fig. 7 shows v_x for a 5 mm axial depth, which is predicted to be unstable in Fig. 5. The same four C values were evaluated and the spindle speed was 11000 rpm. It is observed that the v_x amplitude is now sensitive to C. This provides the motivation for calibrating the C value using measured workpiece velocity during unstable cutting tests.

To calibrate C, a test point of {11,000 rpm, 10 mm} was selected for a single milling experiment. This axial depth was chosen to ensure that unstable behavior was obtained. The process damping coefficient was varied to obtain agreement between the simulated and measured v_x. The results for $C = 4.33 \times 10^5$ N/m are displayed in Fig. 8. It is observed that the cutting conditions are unstable; significant content is present at frequencies other than the tooth passing frequency (550 Hz) and its integer multiples (harmonics).

Given the calibrated C value, a stability map was generated using a grid of time domain simulations from 2000 rpm to 16,000 rpm (50 rpm steps) and 0.5 mm to 15 mm (0.5 mm steps). The values from Tables 1 and 2 were used for the 6.35 mm radial depth, 0.025 mm feed per tooth down milling simulations. To automatically label stable and unstable cutting conditions, the once-per-revolution sampling metric, M,

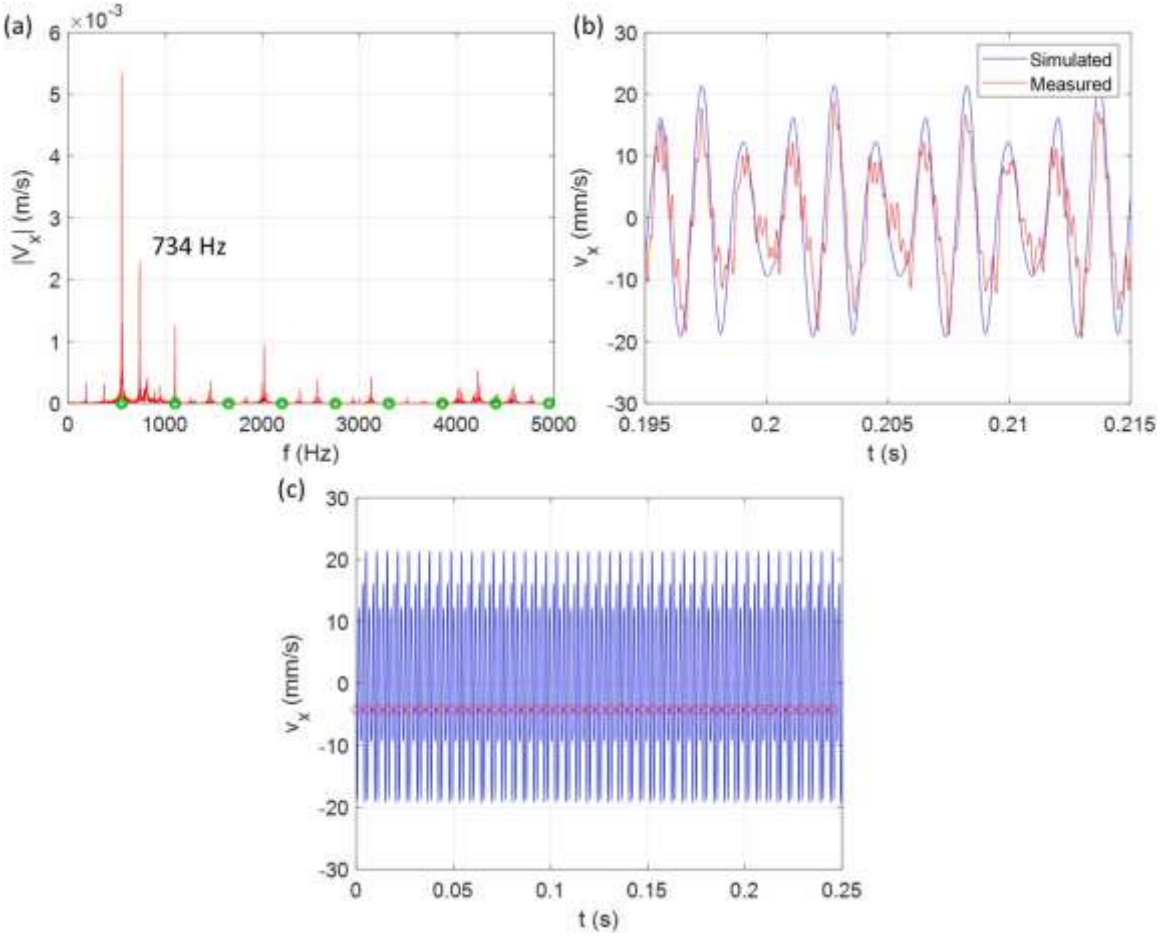

Fig. 10. (a) Magnitude of frequency content for the measured workpiece velocity at {11,000 rpm, 5 mm}. (b) Comparison of measured and simulated workpiece v_x for $C = 4.33 \times 10^5$ N/m. (c) Predicted velocity with once-per-revolution sampling (red circles). Because the samples repeat, stable behavior is identified.

described in [36] was implemented. The metric quantifies the repeatability in the once-per-revolution samples as shown in Eq. 14, where x_s is the once-per-revolution sampled workpiece displacement in the x direction and N is the number of points.

$$M = \frac{1}{N}\sum_{i=2}^{N}\left(x_s(i) - x_s(i-1)\right) \quad (14)$$

For stable behavior (forced vibration), the samples repeat so the M value should approach zero under steady-state conditions. A threshold of 1 µm was selected to accommodate computational resolution in the time domain simulation. The stability map is displayed in Fig. 9, where spindle speed-axial depth combinations below the boundary have M values less than 1 µm. In comparison to Fig. 5, it is observed that the allowable axial depth without chatter is increased with a larger effect at lower spindle speeds, as expected.

To evaluate the process damping coefficient and Fig. 9 stability map, additional tests were performed at various {Ω, b} combinations and the measured velocity was compared to the simulated velocity. Fig. 10 displays the results for {11,000 rpm, 5 mm}. As predicted, the cut is stable. The additional frequency content in panel (a) at 734 Hz occurs at the fourth harmonic of the runout frequency (i.e., spindle speed). The effect of runout is also observed in the time domain v_x from panel (b), where the amplitudes vary with tooth passage and repeat every three teeth.

Fig. 11 shows the results for {11,000 rpm, 15 mm}. As predicted by Fig. 9, the cut is unstable and the 802.6 Hz chatter frequency is identified. Note the increased velocity amplitude relative to Figs. 8 and 10 due to chatter at the higher axial depth.

In addition to the 11,000 rpm tests, experiments were also performed at 2000 rpm and 15,000 rpm; the axial depth was 10 mm in each case. For the 15,000 rpm case shown in Fig. 12, the tooth passing frequency is 750 Hz. Because it is close to the platform natural frequency, this {Ω, b} combination is near a local maximum in the stability boundary and the chatter frequency is coincident with the tooth passing frequency. Note the large velocity amplitude for this case.

The 2000 rpm results are displayed in Fig. 13. Due to the process damping effect, this cut is within the stable zone in Fig. 9 and the prediction is confirmed by the results. In panel (a), the 799.6 Hz peak is aligned with a tooth passing harmonic; the local amplification is caused by the platform vibration mode in the x direction. In panel (b), the simulated velocity underpredicts the measured velocity, but the signals are similar and, more importantly, stable conditions are correctly predicted. Note the small velocity amplitude even though the axial depth is
10 mm.

To conclude the experiments, the cutting direction was switched from down to up milling and the {11,000 rpm, 10 mm} test was repeated. The radial depth and feed per tooth were the same. The unstable results are shown in Fig. 14. Good agreement between simulation and measurement is seen for the same $C = 4.33 \times 10^5$ N/m process damping coefficient. Note that the velocity amplitude is different than the down milling result in Fig. 8.

5. Conclusions

This paper described a process damping force model, where the coefficient was calibrated using an in situ measurement of velocity during

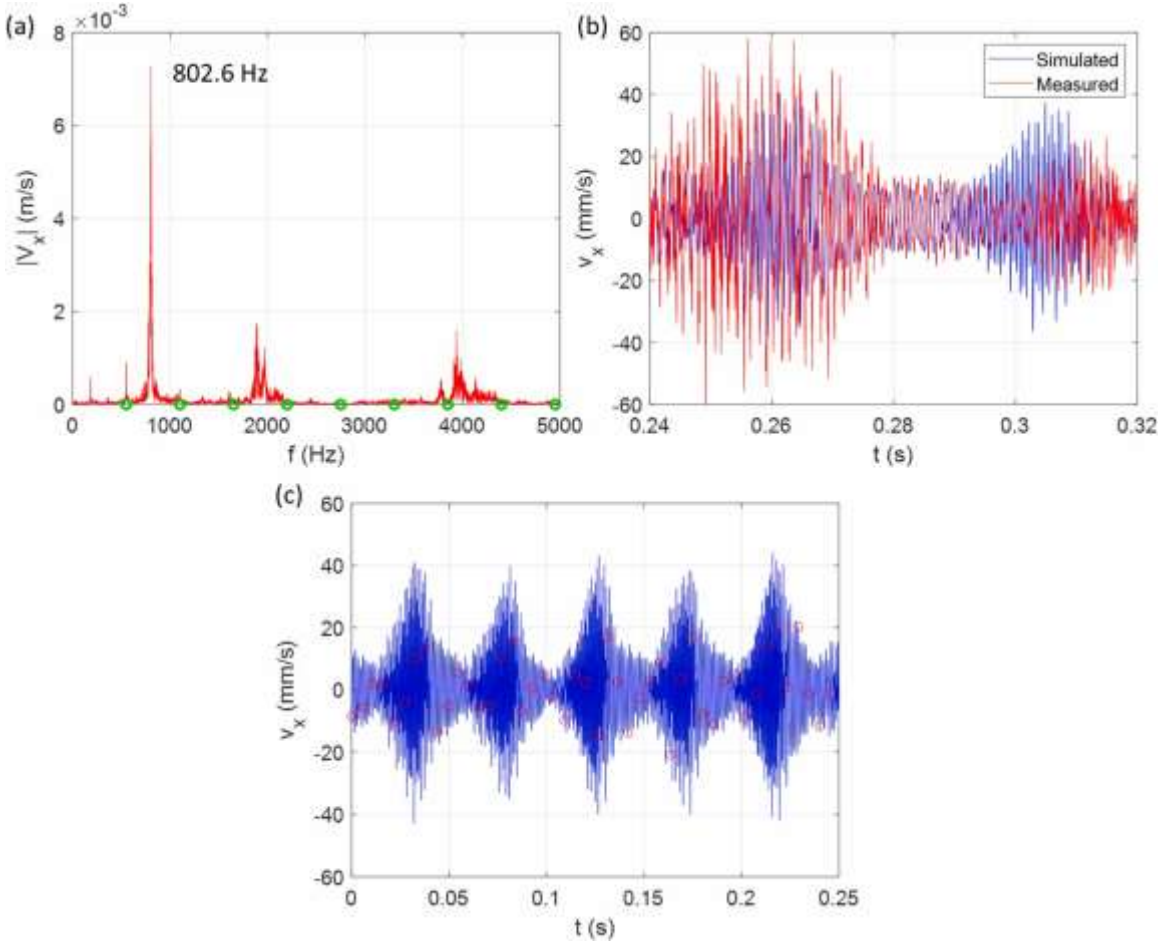

Fig. 11. (a) Magnitude of frequency content for the measured workpiece velocity at {11000 rpm, 15 mm}. (b) Comparison of measured and simulated workpiece v_x for $C = 4.33 \times 10^5$ N/m. (c) Predicted velocity with once-per-revolution sampling (red circles). Because the samples do not repeat, unstable behavior is identified.

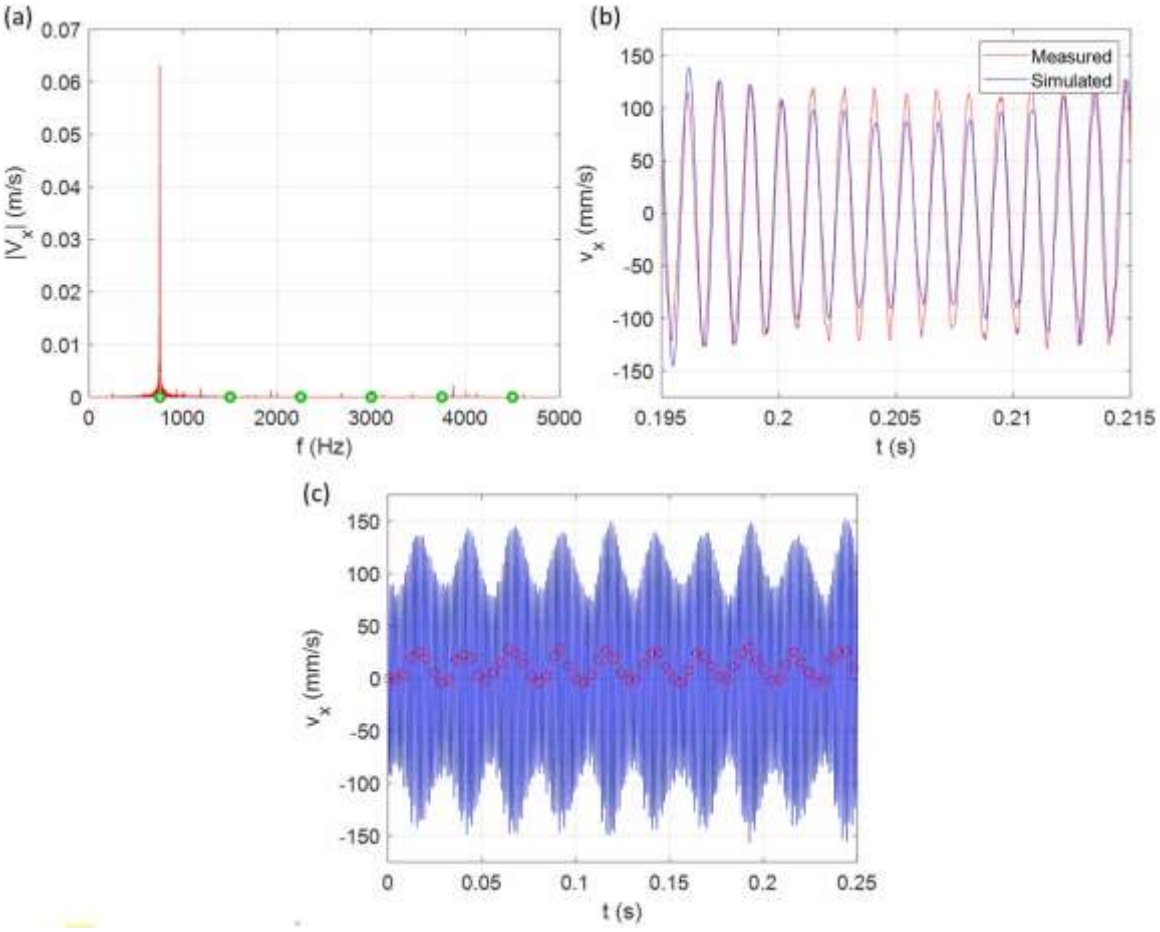

Fig. 12. (a) Magnitude of frequency content for the measured workpiece velocity at {15,000 rpm, 10 mm}. (b) Comparison of measured and simulated workpiece v_x for $C = 4.33 \times 10^5$ N/m. (c) Predicted velocity with once-per-revolution sampling (red circles). Because the samples do not repeat, unstable behavior is identified.

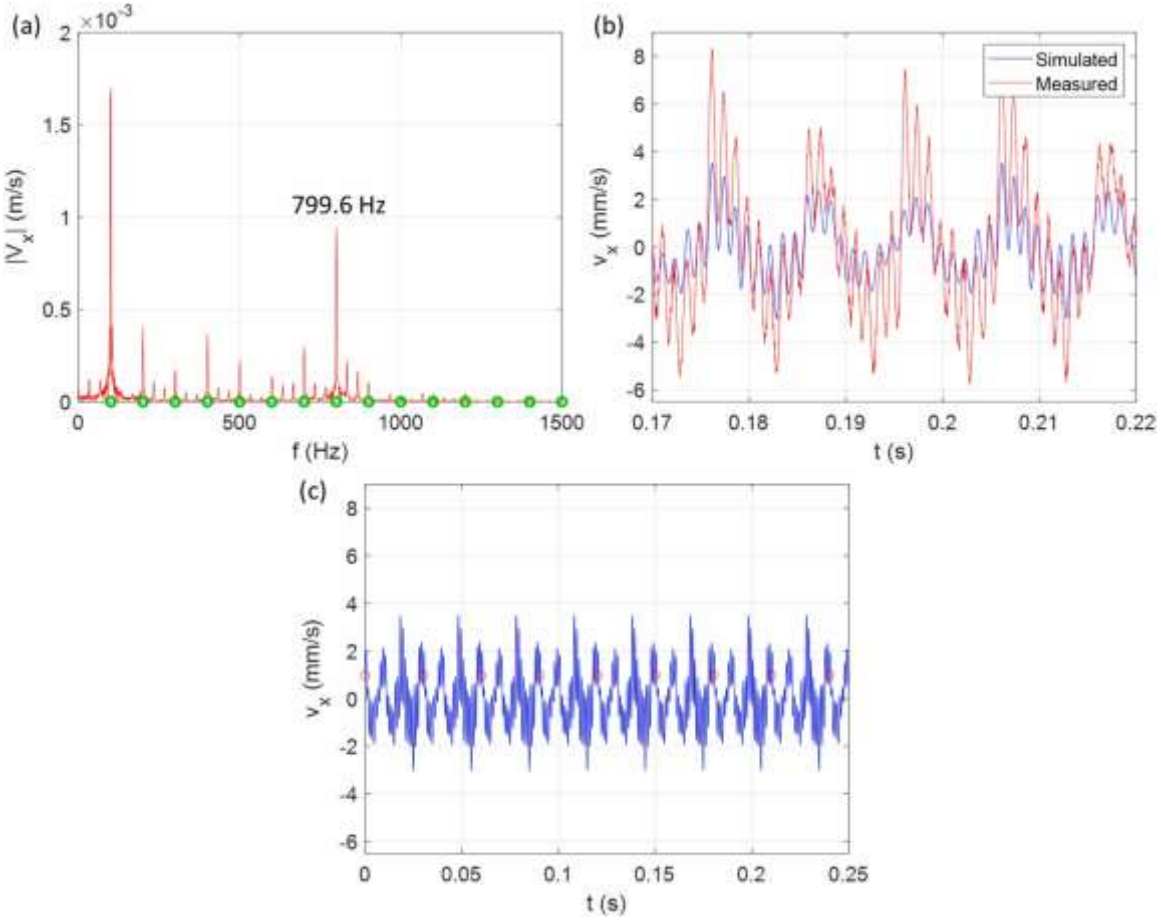

Fig. 13. (a) Magnitude of frequency content for the measured workpiece velocity at {2000 rpm, 10 mm}. (b) Comparison of measured and simulated workpiece v_x for $C = 4.33 \times 10^5$ N/m. (c) Predicted velocity with once-per-revolution sampling (red circles). Because the samples repeat, stable behavior is identified.

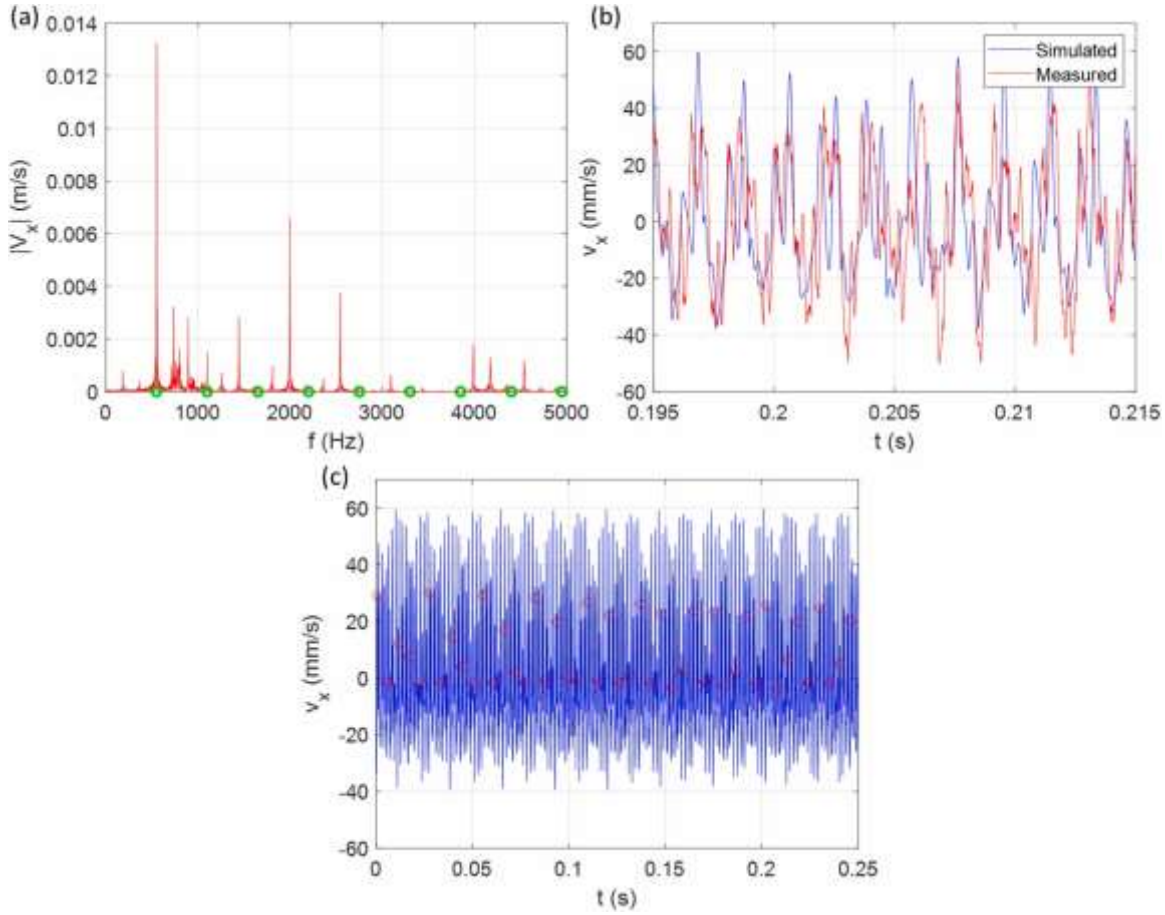

Fig. 14. (a) Magnitude of frequency content for the measured workpiece velocity at {11,000 rpm, 10 mm} and up milling conditions. (b) Comparison of measured and simulated workpiece v_x for $C = 4.33 \times 10^5$ N/m. (c) Predicted velocity with once-per-revolution sampling (red circles). Because the samples do not repeat,

unstable behavior is identified.

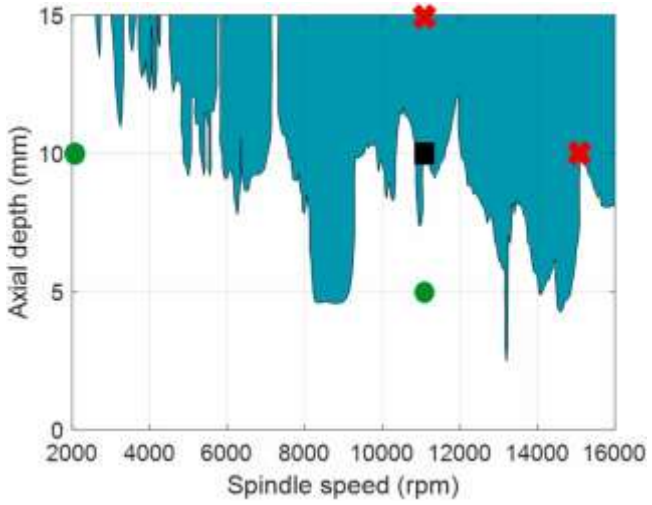

Fig. 15. Summary of 50 % radial immersion experimental results. The process damping coefficient was calibrated at the test point indicated by the black square. The green circles identify stable tests and the red × symbols identify unstable tests. The stability map was calculated for down milling. An additional test was performed at the calibration test point for up milling; the result was unstable as predicted (not shown). an unstable milling test. A flexure-based platform was implemented to enable workpiece velocity measurement using a laser Doppler vibrometer. The cutting force components, displacements, velocities, and
accelerations of the tool and workpiece were calculated by time domain simulation. The simulated velocity was compared to the measured velocity for unstable (chatter) cutting conditions, where it was shown that the sensitivity of the velocity to the process damping coefficient is higher for unstable conditions. By selecting the process damping coefficient to provide agreement between the simulated and measured velocities, calculation of a stability map using the calibrated process damping coefficient for a grid of time domain simulations was enabled. The modeling approach was described and experimental results were provided for various spindle speeds-axial depth combinations based on the stability map.

In this initial study, the coefficient calibration was performed at one spindle speed-axial depth combination with a velocity magnitude of approximately 30 mm/s. Validation testing was competed at five additional spindle speed-axial depth combinations with velocity magnitudes of less 10 mm/s to approximately 150 mm/s. Good agreement was obtained between measured and simulated velocities. Accurate stability predictions and characterization of the process damping effect were also observed. A summary of the testing is provided in Fig. 15. The machining conditions were 50 % radial immersion for both down (climb) and up (conventional) milling. Low radial immersion, which can exhibit complex bifurcation behaviors, was not tested. While this paper does not provide a definitive study, the hypothesis based on the preliminary data is that a single coefficient calibrated using measured velocity under unstable cutting conditions may be sufficient to predict the process damping behavior for a selected tool-material combination. Further testing will be required to establish whether this single coefficient with velocity calibration hypothesis has merit.

CRediT authorship contribution statement

Jose Nazario: Visualization, Validation, Software, Methodology, Investigation, Formal analysis, Data curation. **Dylan Pollard:** Visualization, Validation, Software, Methodology, Investigation, Formal analysis, Data curation. **Tyler Woodard:** Investigation, Data curation. **Junbeom Son:** Investigation, Data curation. **Tony Schmitz:** Writing – review & editing, Writing – original draft, Visualization, Validation, Supervision, Software, Resources, Project administration, Methodology, Investigation, Funding acquisition, Formal analysis, Conceptualization. **Michael Gomez:** Supervision, Resources, Methodology, Investigation, Conceptualization.

Declaration of Competing Interest

The authors declare that they have no known competing financial interests or personal relationships that could have appeared to influence the work reported in this paper.

Acknowledgements

This manuscript has been authored in part by UT-Battelle, LLC under Contract No. DE-AC05–00OR22725 with the DOE. The US Government retains and the publisher, by accepting the article for publication, acknowledges that the US Government retains a non-exclusive, paid-up, irrevocable, world-wide license to publish or reproduce the published form of this manuscript, or allow others to do so, for United States Government purposes. The DOE will provide public access to these results of federally sponsored research in accordance with the DOE Public Access Plan (http://energy.gov/downloads/doe-public-access-plan). The authors also acknowledge support from the NSF Engineering Research Center for Hybrid Autonomous Manufacturing Moving from Evolution to Revolution (ERC-HAMMER) under Award Number EEC- 2133630.

References

[1] Altintas Y, Weck M. Chatter stability of metal cutting and grinding. CIRP Ann 2004; 53(2):619–42.
[2] Schmitz T, Smith KS. Machining Dynamics: Frequency Response to Improved Productivity, Second Edition. New York, NY: Springer,; 2019.
[3] Altintas Y, Stepan G, Budak E, Schmitz T, Kilic ZM. Chatter stability of machining operations. J Manuf Sci Eng 2020;142(11):110801.
[4] Sisson TR, Kegg RL. An explanation of low-speed chatter effects. ASME J Eng Ind 1969;91(4):951–8.
[5] Wallace PW, Andrew C. Machining forces: Some effects of tool vibration. J Mech Eng Sci 1965;7(2):152–62.
[6] Peters J, Vanherck P, Van Brussel H. The measurement of the dynamic cutting coefficient. Ann CIRP 1971;21(2):129–36.
[7] Hoshi T. Cutting dynamics associated with vibration normal to cut surface. Ann CIRP 1972;21(1):101–2.
[8] Tlusty J. Analysis of the state of research in cutting dynamics. Ann CIRP 1978;27: 583–9.
[9] Tlusty J, Ismail F. Basic nonlinearity in machining chatter. Ann CIRP 1981;30(1): 299–304.
[10] Montgomery D, Altintas Y. Mechanism of cutting force and surface generation in dynamic milling. Trans ASME J Eng Ind 1991;113:160–8.
[11] Chiou RY, Liang SY. Chatter stability of a slender cutting tool in turning with tool wear effect. Int J Mach Tools Manuf 1998;38(4):315–27.
[12] Clancy BE, Shin YC. A comprehensive chatter prediction model for face turning operation including tool wear effect. Int J Mach Tools Manuf 2002;42(9):1035–44.
[13] Huang CY, Wang JJJ. Mechanistic modeling of process damping in peripheral milling. Transactions of ASME. J Manuf Sci Eng 2007;129(1):12–20.
[14] Budak E, Tunc LT. A new method for identification and modeling of process damping in machining. J Manuf Sci Eng 2009;131(5):051019.
[15] Budak E, Tunc LT. Identification and modeling of process damping in turning and milling using a new approach. CIRP Ann 2010;59(1):403–8.
[16] Sellmeier V, Denkena B. High speed process damping in milling. CIRP J Manuf Sci Technol 2012;5(1):8–19.
[17] Tunç LT, Budak E. Effect of cutting conditions and tool geometry on process damping in machining. Int J Mach Tools Manuf 2012;57:10–9.
[18] Tyler CT, Schmitz TL. Analytical process damping stability prediction. J Manuf Process 2013;15(1):69–76.
[19] Karandikar JM, Tyler CT, Schmitz TL. Process damping coefficient identification using Bayesian inference. Proc NAMRI/SME 2013;41.
[20] Karandikar JM, Tyler CT, Abbas A, Schmitz TL. Value of information-based experimental design: Application to process damping in milling. Precis Eng 2014; 38(4):799–808.
[21] Ahmadi K, Altintas Y. Identification of machining process damping using output- only modal analysis. J Manuf Sci Eng 2014;136(5):051017.
[22] Tyler CT, Troutman JR, Schmitz TL. A coupled dynamics, multiple degree of freedom process damping model, Part 1: Turning. Precis Eng 2016;46:65–72.
[23] Tyler CT, Troutman JR, Schmitz TL. A coupled dynamics, multiple degree of freedom process damping model, Part 2: Milling. Precis Eng 2016;46:73–80.
[24] Gurdal O, Ozturk E, Sims ND. Analysis of process damping in milling. Procedia CIRP 2016;55:152–7.
[25] Wan M, Feng J, Ma YC, Zhang WH. Identification of milling process damping using operational modal analysis. Int J Mach Tools Manuf 2017;122:120–31.

[26] Tuysuz O, Altintas Y. Analytical modeling of process damping in machining. J Manuf Sci Eng 2019;141(6):061006.
[27] Cornelius A, Karandikar J, Tyler C, Schmitz T. Process damping identification using Bayesian learning and time domain simulation. J Manuf Sci Eng 2024;146(8).
[28] Altintas Y, Eynian M, Onozuka H. Identification of dynamic cutting force coefficients and chatter stability with process damping. CIRP Ann 2008;57(1): 371–4.
[29] Das MK, Tobias SA. The relation between the static and the dynamic cutting of metals. Int J Mach Tool Des Res 1967;7(2):63–89.
[30] Lee BY, Tarng YS, Ma SC. Modeling of the process damping force in chatter vibration. Int J Mach Tools Manuf 1995;35(7):951–62.
[31] Honeycutt A, Schmitz T. A numerical and experimental investigation of period-n bifurcations in milling. J Manuf Sci Eng 2017;139(1):011003.
[32] Dombovari Z, Barton DA, Wilson RE, Stepan G. On the global dynamics of chatter in the orthogonal cuttingmodel. Int J Non-Linear Mech 2011;46(1):330–8.
[33] Moradi H, Vossoughi G, Movahhedy MR. Bifurcation analysis of nonlinear milling process with tool wear and process damping: sub-harmonic resonance under regenerative chatter. Int J Mech Sci 2014;85:1–19.
[34] Gomez M, Schmitz T. Low-cost, constrained-motion dynamometer for milling force measurement. Manuf Lett 2020;25:34–9.
[35] Altintas Y, Budak E. Analytical prediction of stability lobes in milling. CIRP Ann 1995;44(1):357–62.
[36] Honeycutt A, Schmitz T. A new metric for automated stability identification in time domain milling simulation. J Manuf Sci Eng 2016;138(7):074501.